Structural health monitoring of grouted connections for offshore wind turbines by means of acoustic emission

Tziavos, Nick; Hemida, Hassan; Dirar, Samir; Papaelias, Mayorkinos; Metje, Nicole; Baniotopoulos, Charalampos

DOI:
10.1016/j.renene.2019.08.114

--Manuscript--

Title: Structural health monitoring of grouted connections for offshore wind turbines by means of acoustic emission: An experimental study

Authors: [1a]Nikolaos I. Tziavos, [1]H. Hemida, [1]S. Dirar, [2]M. Papaelias, [1]N. Metje, [1]C. Baniotopoulos

Affiliations

[1]School of Engineering, Department of Civil Engineering, University of Birmingham, Edgbaston, Birmingham, B15 2TT, UK

[2]School of Metallurgy and Materials, University of Birmingham, Edgbaston, Birmingham, B15 2TT, UK

Number of figures: 23

Number of tables: 3

Highlights

- Quantitative monitoring of the grout condition using Acoustic Emission (AE) is demonstrated.
- A cross-correlation of structural damage progression with identified key performance indicators (KPIs) is presented.
- Analysis of AE data by means of b and Ib-value analysis.

[a] Current address: School of Electronic and Electrical Engineering, University of Bath, Claverton Down, Bath, BA2 7AY, UK

18 **--Manuscript Draft--**

19 **Abstract:** Grouted connections for offshore wind turbines are formed by attaching overlapping
20 steel piles with an ultra-high strength cementitious grout. The structural performance of grouted
21 connections is critical for the substructures in order to exhibit sufficient resistance to
22 environmental loads. The long-term integrity of the grout core can be compromised due to the
23 complex stress states present, leading to unexpected slippage and gaps in the steel-grout interface,
24 grout cracking and water ingress. This paper presents the results of an experimental investigation
25 on damage evolution and failure mechanisms occurring within grouted connections in laboratory-
26 based bending tests using acoustic emission. A parametric analysis of the detected acoustic
27 emission signals has been conducted. The acoustic emission activity has been correlated with load-
28 displacement measurements and the observed specimen failure modes. For the tested grouted
29 connections, the number of acoustic emission hits and the signal duration were employed to
30 identify damage evolution during load application. Root mean square and the ratio of rise time to
31 amplitude were found to be useful key performance indicators for damage prognosis. Finally, an
32 improved b-value analysis has been performed, and the computed drops were well-associated with
33 grout cracking within the connection.

34 **Keywords:** Grouted connection, Offshore wind substructures, Acoustic Emission, Structural
35 health monitoring, Structural integrity, Damage evolution

36

Abbreviations

AE	**A**coustic **E**mission
CSS	**C**umulative **S**ignal **S**trength
GCs	**G**routed **C**onnections
KPIs	**K**ey **P**erformance **I**ndicators
NDT	**N**on-**D**estructive **T**esting
OWT	**O**ffshore **W**ind **T**urbines
PAC	**P**hysical **A**coustics **C**orporation
RMS	**R**oot **M**ean **S**quare
SHM	**S**tructural **H**ealth **M**onitoring
TP	**T**ransition **P**iece
UHPC	**U**ltra **H**igh **P**erformance **C**ementitious

1 Introduction

Grouted connections (GCs) are commonly employed in fixed-bottom offshore wind turbine (OWT) substructures such as monopiles, jackets or tripods. They are formed by filling the annuli between concentric overlapping tubular steel piles – the monopile and the transition piece (TP), with an ultra-high performance cementitious (UHPC) grout. GCs are often referred as pile-to-sleeve connections due to their arrangement and are constructed to accommodate the transition from the foundation pile to the tower. Their structural performance is critical to the substructure, contributing significantly to the ability of the structure to withstand environmental loads arising from wind, waves and sea currents.

In 2009, monopile inspections revealed TP settlements and the overall performance of GCs was called in question (Lotsberg, 2013). Inspections of monopiles around Europe revealed TPs sliding by several millimetres (Dallyn et al., 2016; Tziavos et al., 2016) requiring costly mitigation measures (Iliopoulos et al., 2016). Other typical defects that were reported, included grout cracking and gaps at the top of the GC (Brett et al., 2018). To address these issues, extensive maintenance activities were required offshore; operators applied ad hoc solutions on a case by case basis, including the installation of internal brackets to prevent further TP sliding (Brett et al. 2018). However, accessibility to OWT locations is affected by weather conditions and maintenance tasks require complete shutdown of the generator (Márquez et al., 2012; Shafiee and Sorensen, 2017), leading to significant expenditure.

Nowadays, minimising unnecessary maintenance expenditure due to high costs and also enhancing the reliability of OWT substructures are some of the main challenges for the offshore wind sector (Shafiee et al., 2016; Martinez-Luengo et al., 2016). In order to address these challenges, a transition to condition and/or predictive-based maintenance is necessary, compared to corrective and preventive strategies, which are commonly employed. Condition-based

maintenance is based on the detection, identification and monitoring of damage evolution with time. Therefore, the operators can schedule maintenance activities more effectively reducing the operation and maintenance costs for OWTs by a significant margin (Yang et al., 2013; Rolfes et al., 2014; Marugan et al., 2016; Márquez et al., 2016; Artigao, et al., 2018). However, condition-based maintenance is yet to be employed at a satisfactory level leading to higher cost for wind power generation. Considering the aforementioned and the lack of expert knowledge and experience on the long-term behaviour of UHPC grouts the need for effective monitoring tools for GCs is evident. For this purpose, structural health monitoring (SHM) is in the forefront for damage detection and evaluation, aiming to aid decision making by diagnosing the structural state of the element under examination, improving the reliability of OWT substructures (Martinez-Luengo et al., 2016).

The first application of Non-Destructive Testing (NDT) on GCs is presented in Iliopoulos et al. (2016). The authors extracted grout cores from in-service offshore monopile connections. A combination of ultrasonic pulse velocity and X-rays was employed to evaluate the condition of the samples based on their location across the length of the GC, showing promising results. Häckell et al. (2017) presented a global approach using vibration-based monitoring of a GC while, a pilot study on the applicability of electromechanical impedance spectroscopy for defect detection was conducted by Moll (2018). Driven by the reported failures, Brett et al. (2018) presented an ultrasonic-based inspection method which was verified with small-scale steel-grout-steel samples and field trials. Despite the limited number of research studies focusing on GCs, promising results have been reported, encouraging the use of SHM approaches for inspection and monitoring, to prevent future failures and reduce operational and maintenance expenditure.

Taking into consideration the offshore conditions and the type of loads exerted on an OWT, it is of great importance to be able to monitor the GC continuously. Acoustic Emission (AE) is an alternative NDT method with unexplored potential, which can be used remotely for real time monitoring (Duthie and Gabriels, 2014). AE is a passive technique which is employed to detect

99 elastic energy changes caused by external motives (Grosse and Ohtsu, 2008). Events such as
100 cracking or debonding release energy waves (Martinez-Luengo et al., 2016), making AE a potential
101 candidate for monitoring a GC. Some of the advantages of AE include ease of application, high-
102 resolution tracking of cracking events and real time monitoring capabilities. Nonetheless, post-
103 processing can be a tedious task due to lack of a unified approach and data analysis being
104 dependent on acquisition systems. The use of AE for damage detection has already been employed
105 for monitoring OWT blades (Jungert, 2008). In addition, it has been used in a variety of civil
106 engineering applications to capture crack growth or degradation of brittle material. Specifically,
107 for structures where cement-based material is present, AE focuses on damage quantification,
108 source localisation and identification. Examples of such research works can be found in the
109 literature (see, e.g., Farhidzadeh et al., 2013; Sagar and Rao, 2014; Li et al., 2017; Shi et al., 2018).
110 This paper presents the results of a laboratory-based experimental campaign on the
111 feasibility of AE for damage detection and condition evaluation on GCs. The analysis of the
112 acquired AE data is performed by means of waveform parameters utilizing statistical tools to
113 investigate the implementation of such approaches in SHM systems for OWTs. Several AE signal
114 features are examined as Key Performance Indicators (KPIs) for damage assessment within a GC
115 and crack detection. Section 2 introduces the experimental campaign and Section 3 presents the
116 processing methodology. In Section 4 the experimental results are presented and discussed,
117 followed by the conclusions in Section 5.

118 # 2 Experimental testing

119 The following sections summarize the key specifics of the laboratory-based experiments
120 carried out at the Structural Laboratories of the University of Birmingham, UK. A detailed
121 description of the experimental procedures that were followed is given in Tziavos (2019).

2.1 Geometry of specimens

Two identical cylindrically-shaped GCs (GC-1, GC-2) were designed and tested in bending under monotonic and fatigue loads. Within the scope of this paper, only the ultimate strength tests are considered for benchmarking purposes, aiming to identify KPIs for damage monitoring and crack detection within the grout core. The pile and sleeve were fabricated from S275 steel grade and circumferential square-profiled shear keys were fillet-welded across the length of the grouted region in overlapping positions, resulting in a total of four shear key pairs. The connection was achieved by pressure pumping an UHPC grout – Ducorit© S5R (Densit, 2018), in the annuli between the overlapping tubulars. The dimensions of the parts forming each GC are given in Table 1. The total span of the tested specimens was approximately 4.5 m with a total overhang of 200 mm.

Table 1: Dimensions of GC specimens

Notation (Units)	Pile	Sleeve	Grout
Length, L (mm)	2550	2550	610
Diameter (mm)	406	473.8	450.8
Thickness (mm)	8	11.1	22.4

Both specimens were grouted in a vertical arrangement depicting realistic grouting conditions and were left to cure in an upright position for three days. Subsequently, the specimens were supported horizontally until the test day. In order to overcome space constraints during curing, the specimens were prepared at different dates. The compressive strength of the grout was determined for each specimen from cubic samples as per BS EN 12390-3:2009 (BSI, 2009) on the day of testing. The average compressive strength of both specimens on the day of testing was 125.4 MPa.

2.2 Test set-up and loading protocol

The specimens were tested in a 4-point bending configuration as illustrated in Figure 1. The load was applied to the specimens via a hydraulic jack and a load cell was used to record it. The hydraulic machine was load-controlled, and a spreader beam was used to distribute the load to the specimen on two semi-circular external flanges. It should be noted that the selected loading scheme is not entirely representative of the loads on GCs, however bending moments are the dominant effects in an offshore environment for monopiles. Furthermore, it has been recently confirmed that not only monopiles, but also modern jackets experience far more bending loads than previously accounted for in the design process (Marion et al., 2018). This is a result of the expansion of OWTs to greater depths, leading to far more vertical than inclined piles. In addition, the selected test set-up provokes failure mechanisms that have been previously reported in experimental (Willke, 2013; Chen et al., 2018) and numerical studies (Tziavos et al., 2019) and were revealed in the inspections on monopile GCs (Brett et al., 2018). Those include grout cracking and crushing, gap opening between the grout and steel interfaces and pile deformations. Details of the experimental set-up are shown in Figure 2.

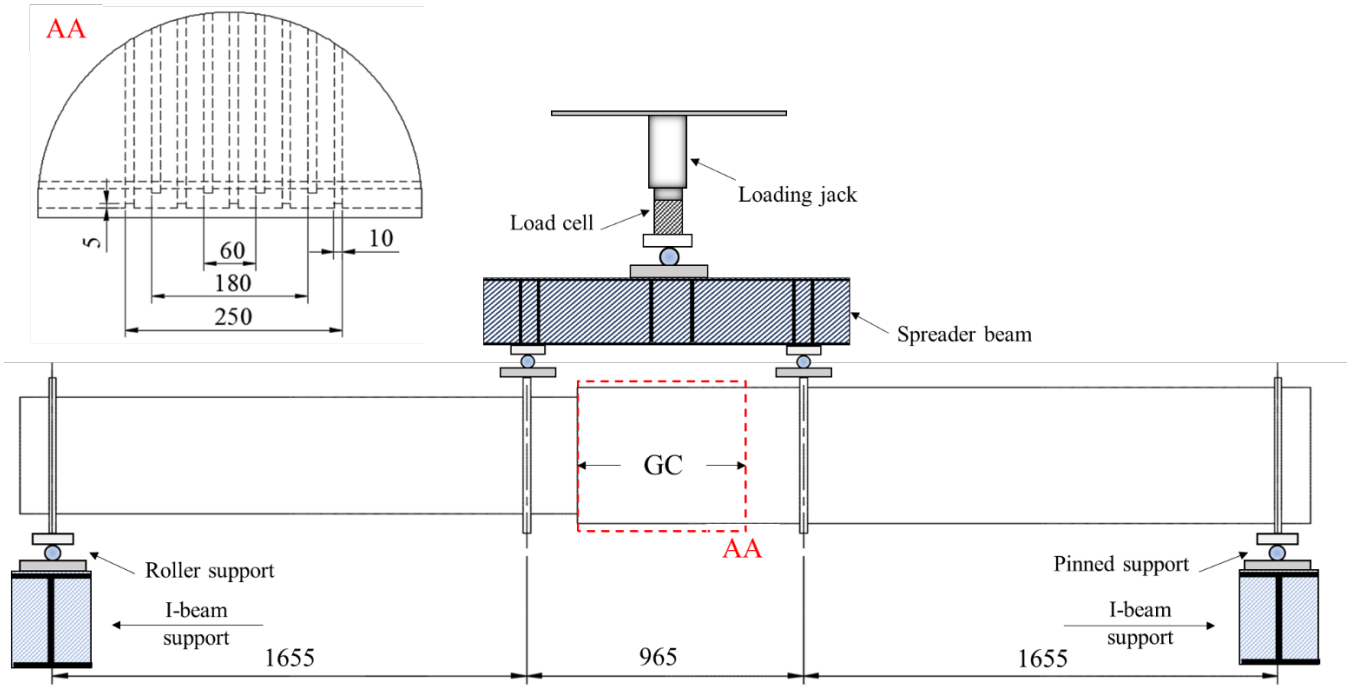

Figure 1: Layout of 4-point bending tests and shear key details (dimensions in *mm*)

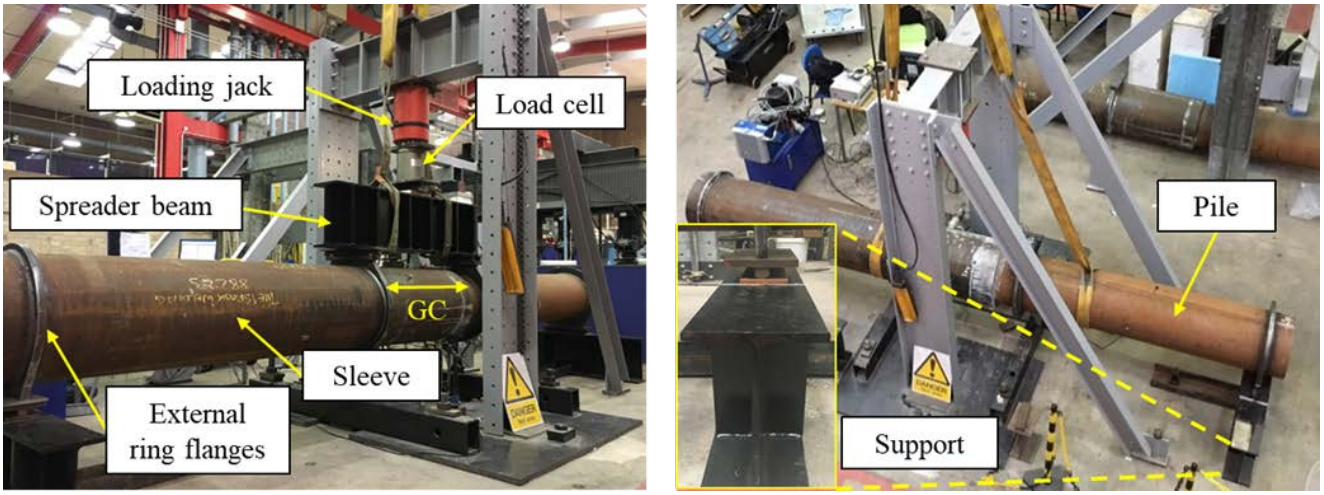

Figure 2: Experiment set-up for GC specimen under bending loads

2.3 AE Instrumentation

The AE activity during the tests was monitored using a 4-channel acquisition system from Physical Acoustics Corporation (PAC), USA. Four AE resonant transducers – PAC50a, were installed at top and bottom locations of the connection and the AEwin™ software was used for

real-time monitoring. Prior to mounting of the sensors, the steel piles were mechanically cleaned. Thereafter, a rapid-setting two-component epoxy was applied to attach them on the outer surface of the sleeve. The transducers have an operating range from 150 kHz to 700 kHz. The signals were amplified using four pre-amplifiers. The gain was set to 40 dB along with a signal filter from 100 kHz to 1000 kHz and a sampling rate of 5MSamples/s. Thresholds of 45 dB and 50 dB was used for GC-1 and GC-2 respectively, to eliminate any background interference from the laboratory environment. The threshold was slightly adjusted in the second test to reduce the number of recorded waveforms. For calibration purposes and to ensure the sensors are properly functioning and spurious hits due to refraction or scattering are not recorded, the Hsu-Nielsen source method was performed at varying distances from each sensor. Displacements of the specimens and steel strains were monitored using Linear Variable Displacement Transducers (LVDTs) and strain gauges. The AE acquisition system is shown schematically in Figure 3 and the installed instrumentation in Figure 4.

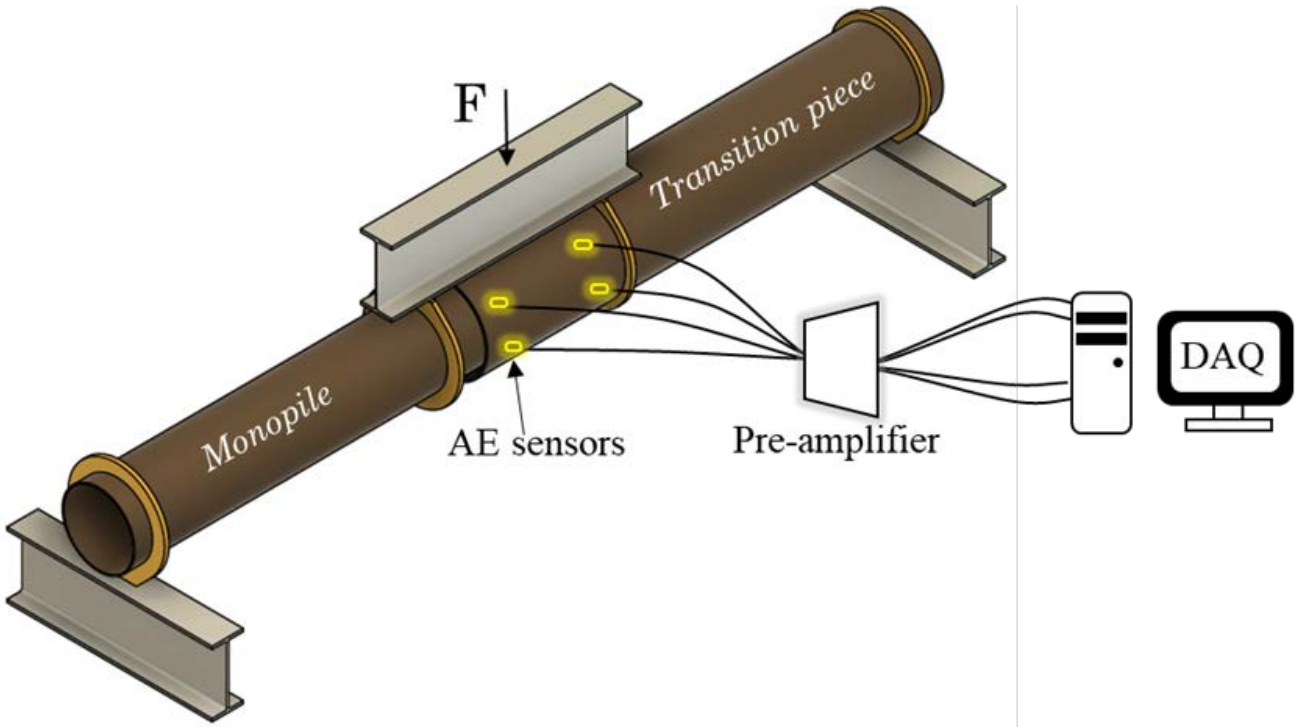

Figure 3: Schematic illustration of AE DAQ system (The AE sensors do not indicate the exact position during the tests)

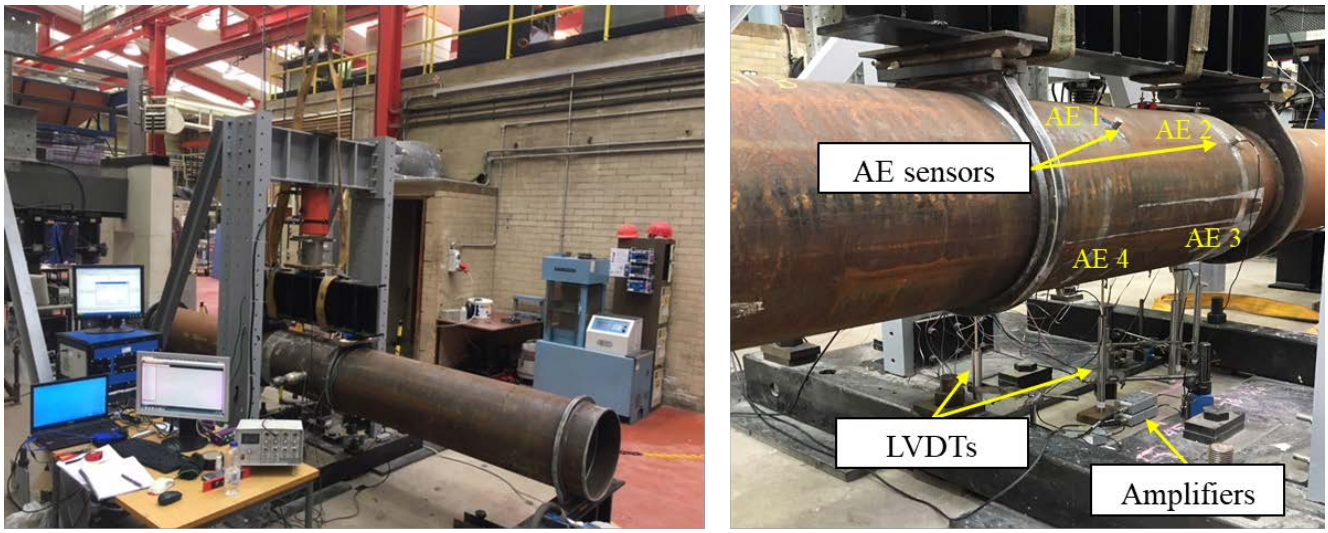

Figure 4: AE acquisition system (left) and installed instrumentation on GC specimen depicting AE sensors, LVDTS and amplifiers (right)

3 Test results and failure modes

184 The results from the 4-point bending tests are shown in Figure 5 using load-deflection
185 curves. For both specimens the presented deflection was measured at the midspan of the GC and
186 the load was acquired from the load cell located on the load application point. The maximum load
187 that was sustained and the corresponding deflections for each GC are given in Table 2. The GCs
188 exhibited a typical ductile-type behaviour comprising an elastic stage up to approximately 400 kN
189 and an elasto-plastic stage until the ultimate load was reached. The tests were stopped once the
190 pile at the compressive side of the GC bottom buckled locally, outside the grouted region and a
191 load-drop followed. A distinct gap at the pile grout interface opened and developed prior to local
192 buckling. The interface gap and the local buckling of the pile are shown in Figure 6.

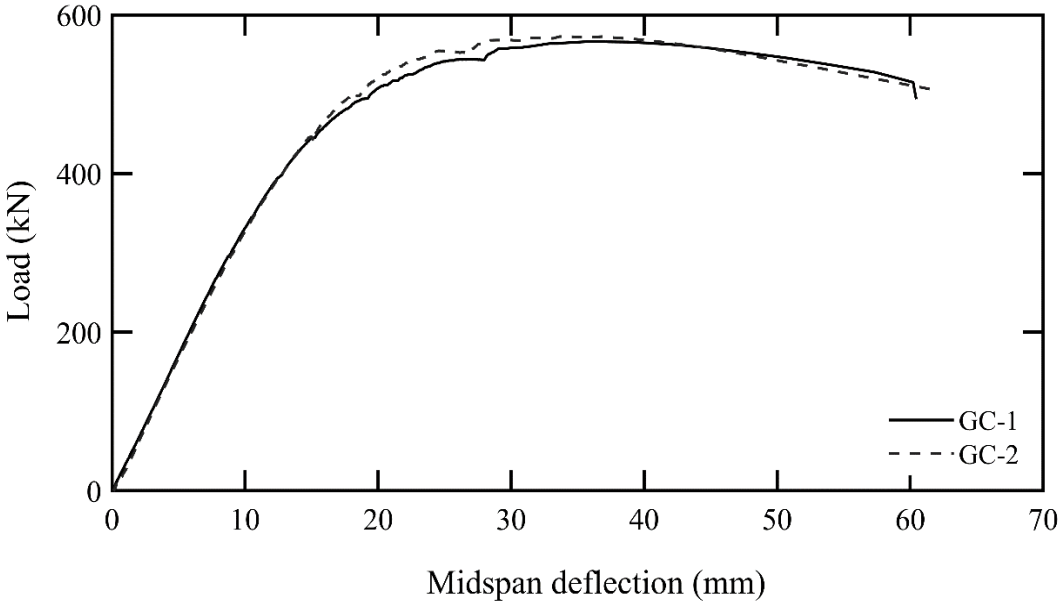

193

194 Figure 5: Load-midspan deflection curves for GC specimens

195

Table 2: Ultimate load for each specimen and corresponding midspan deflection

Specimen ID	Fu (kN)	Δu (mm)
GC-1	566.55	36.20
GC-2	572.60	34.17

Following the tests, visual inspections were carried out to identify the damage that had occurred within the grout core. For this purpose, sections from the sleeve were carefully removed from each specimen. In GCs with circumferential shear keys, cracking and crushing mainly occurs within the region of the effective shear keys. This is due to the shear keys contributing significantly to the load-transfer mechanism, by transferring the loads between the steel tubulars through the grout. This was confirmed and diagonal cracks along with crushed grout was found in the vicinity of the shear keys for both GCs. The diagonal cracking initiated and developed between opposing pile and sleeve shear keys, whereas crushed grout was found on the tip of sleeve shear keys (Figure 7).

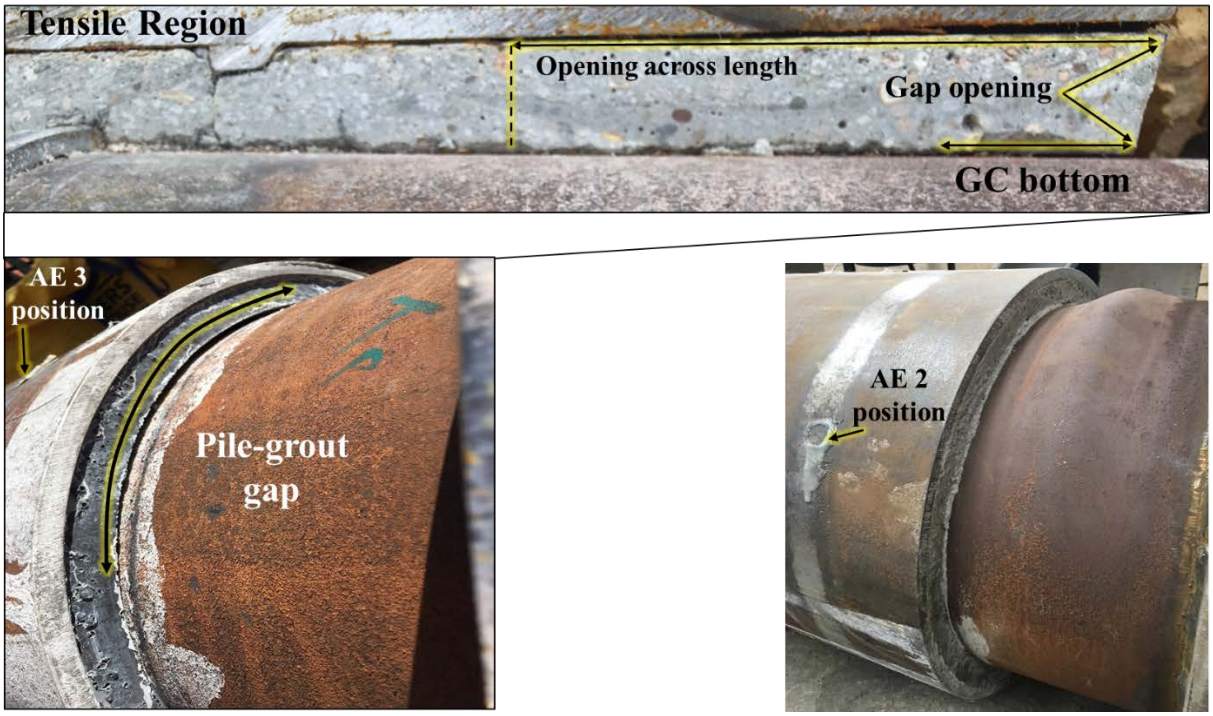

206

207 Figure 6: Interface opening and pile local buckling occurring outside the GC

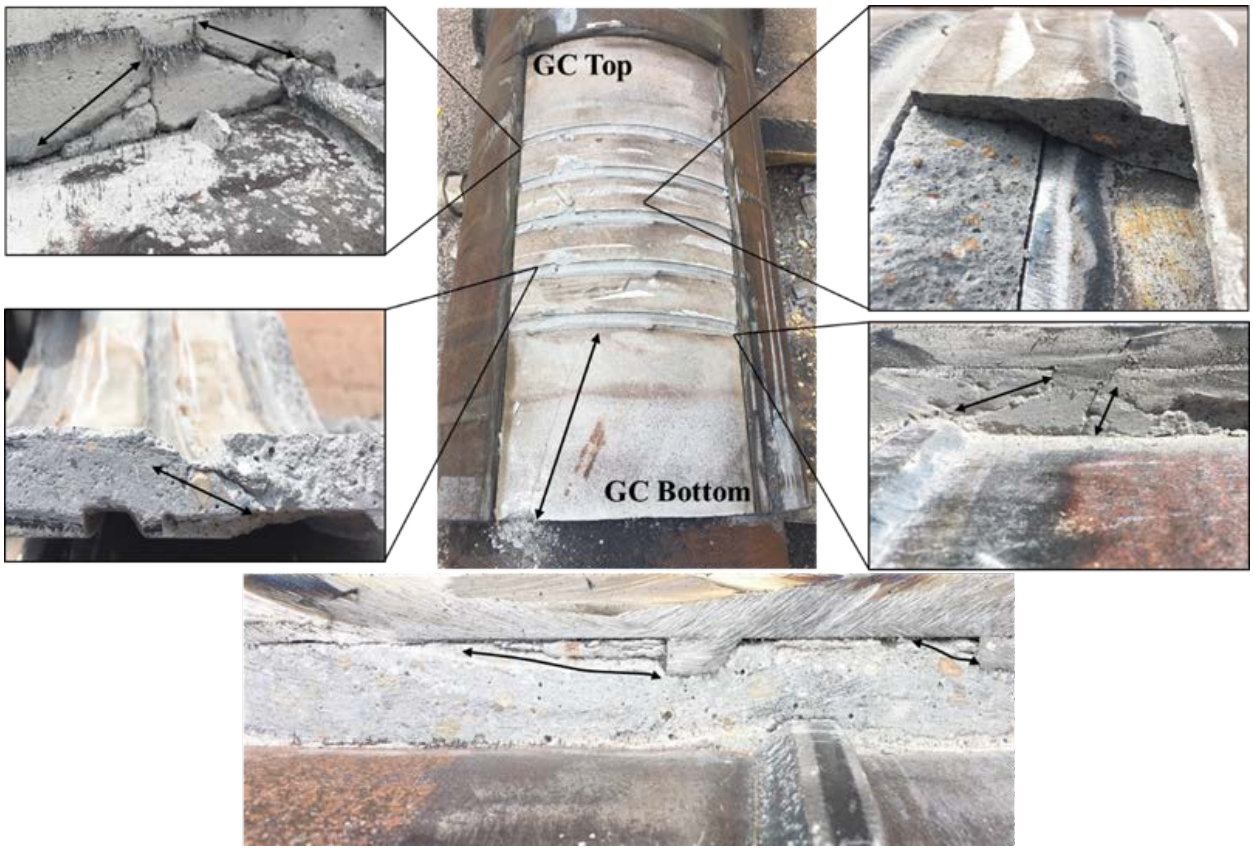

Figure 7: Grout core damage in the shear key region at different locations across the length

4 Damage evolution

For the analysis of the recorded AE signals, a parameter-based processing was elected over signal processing due to the number of recorded waveforms. Characteristic signal features such as peak amplitude, absolute energy or signal strength, are extracted and analysed in the time domain in order to assess damage growth on the specimens. This is a common approach when individual signal processing is not viable (see, e.g., Behnia et al. 2014; Li et al., 2017). From the acquired AE signals, those containing zero PAC energy were subsequently removed from the data sets. PAC energy is an artificial parameter of the acquisition system and it refers to the integral of the signal over its duration, hence such events are not realistic.

4.1 Acoustic Emission activity

For both GCs the sensor that recorded the highest activity was located in the tensile region, towards the bottom of the connection (sensor AE3, see Figure 4). This was expected due to the majority of cracks occurring in the tensile region of the grout core and is also attributed to the sensor being closer to the region where the interface gap and local buckling developed. The total AE activity for the GC specimens under examination increased exponentially with increasing load and this is demonstrated for GC-1 in Figure 8. A large number of hits was recorded, possibly due to the specimen size, roller supports and the UHPC material content (maximum aggregate size ~5 mm), which could have provoked additional AE activity. Initially, small populations of events were recorded which can be associated with the formation of microcracks within the connection and friction at the grout-steel interfaces. The recorded hits increased rapidly once the load reached half of the connection's ultimate capacity. Failure mechanisms that excited the growth of AE signals are related to transition from microcracking to macrocracking and grout crushing in front of the shear keys and once closer to failure to the interface gap along with the local buckling that occurred in the pile.

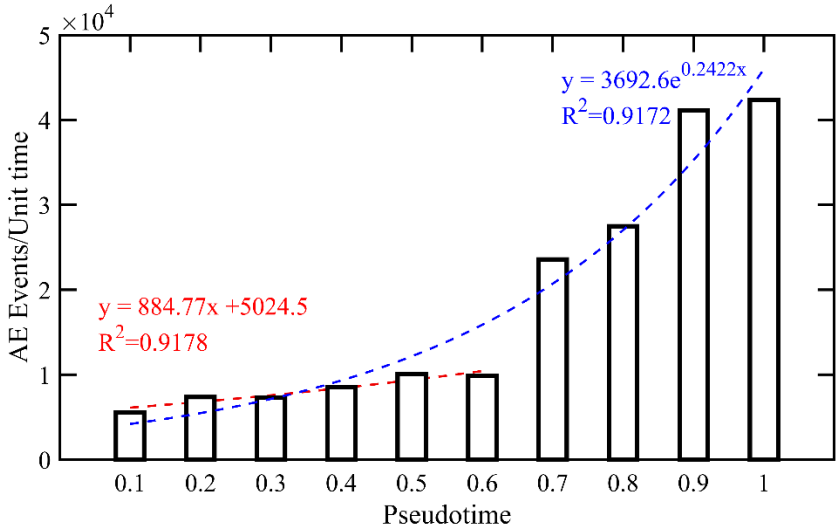

Figure 8: AE events per unit time (GC-1)

The number of events or counts is a useful indicator for the condition of a GC; however, it does not provide specific information on the intensity of the individual signals. In addition, due to the dimensions of the specimens and the test set-up, spurious hits could have been recorded. Therefore, alternative AE parameters can be used to assess the condition of the GCs instead of post-filtering individual events. Typical parameters are the duration of the signal, the cumulative energy, the root mean square (RMS) of voltages or the cumulative signal strength (CSS), which are discussed in the subsequent sections. The scatter diagram in Figure 9 provides some further insight on the condition of the grout during the test. The individual data points represent the duration of the recorded events for the entire time series. It is evident that during the formation of the first microcracks a limited population of low-duration events was captured. Once the severity of damage increases a significantly larger population of hits was recorded. It is suggested that the duration is highly sensitive to damage and contains useful information on the different stages that took place. Figure 9 demonstrates that for both GCs an increase in amplitude is reflected in higher counts. A smaller population of events is presented for GC-2 due to the slightly different settings used in the acquisition set-up in order to reduce the recorded emissions. Nevertheless, the trends for both specimens have similar patterns.

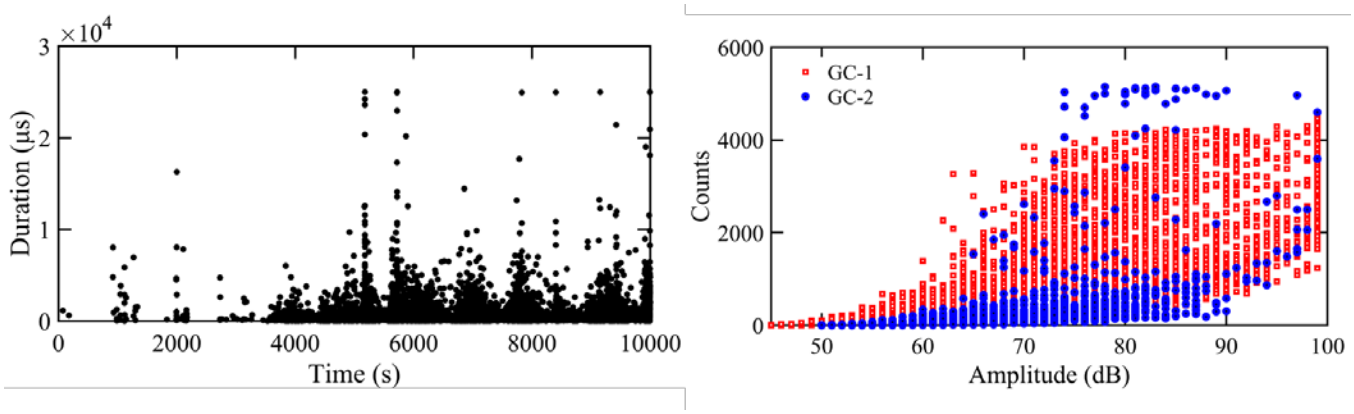

Figure 9: Duration of AE signals against time for GC-2 (left), Cross plot of amplitude against counts (right)

In Figure 10, the cumulative energy from two sensors attached in the opposing regions of the GC (top and bottom) of the grouted connection length is illustrated. It is shown that around 9200 s the gradient of signal energy changes for both sensors. Although, AE2 recorded lower activity, increasing rates and trends were captured simultaneously. The magnitude variation is associated with the proximity of the sensors to regions where more intensive cracking occurred between opposing shear keys. Additionally, AE3 was closely located to the bottom of the connection where de-bonding at the interface occurred prior along with pile buckling.

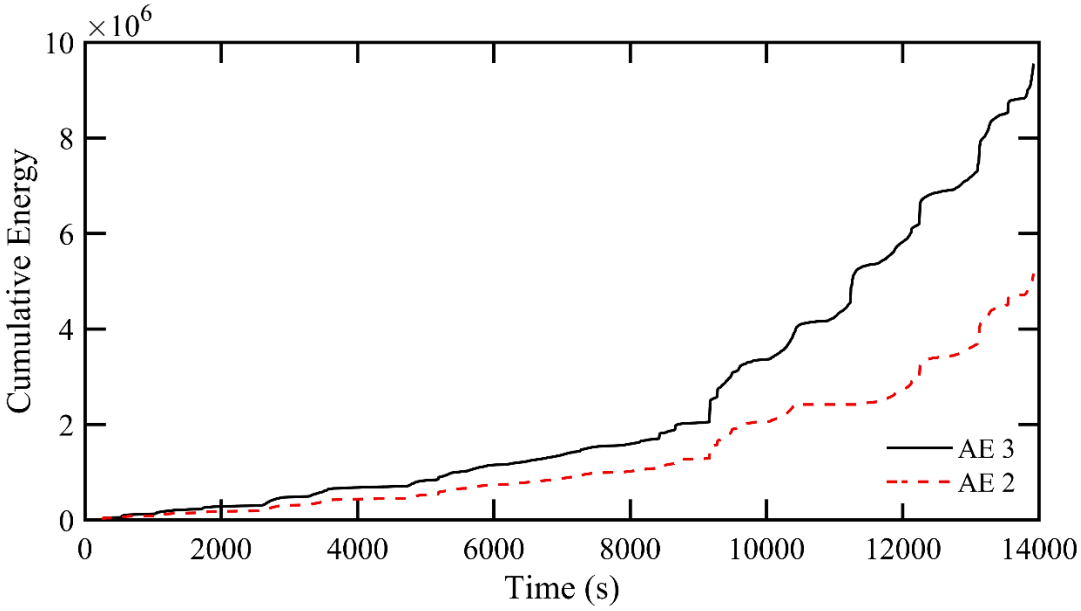

Figure 10: Cumulative energy from GC-1 at the tensile (AE3) and compressive side (AE2)

Higher growth rates correspond to larger AE populations which are commonly associated with damage accumulation. Consequently, steep peaks can be related to macrocracking events especially at earlier stages (Figure 11). An exponential trend in the cumulative energy evolution was also found for GC-2 (Figure 12). This is in agreement with findings reported in earlier studies (Aggelis et al., 2011). The cumulative energy is found to increase with increasing load levels as failure approaches. Identical growth rates and patterns were recorded for both GCs.

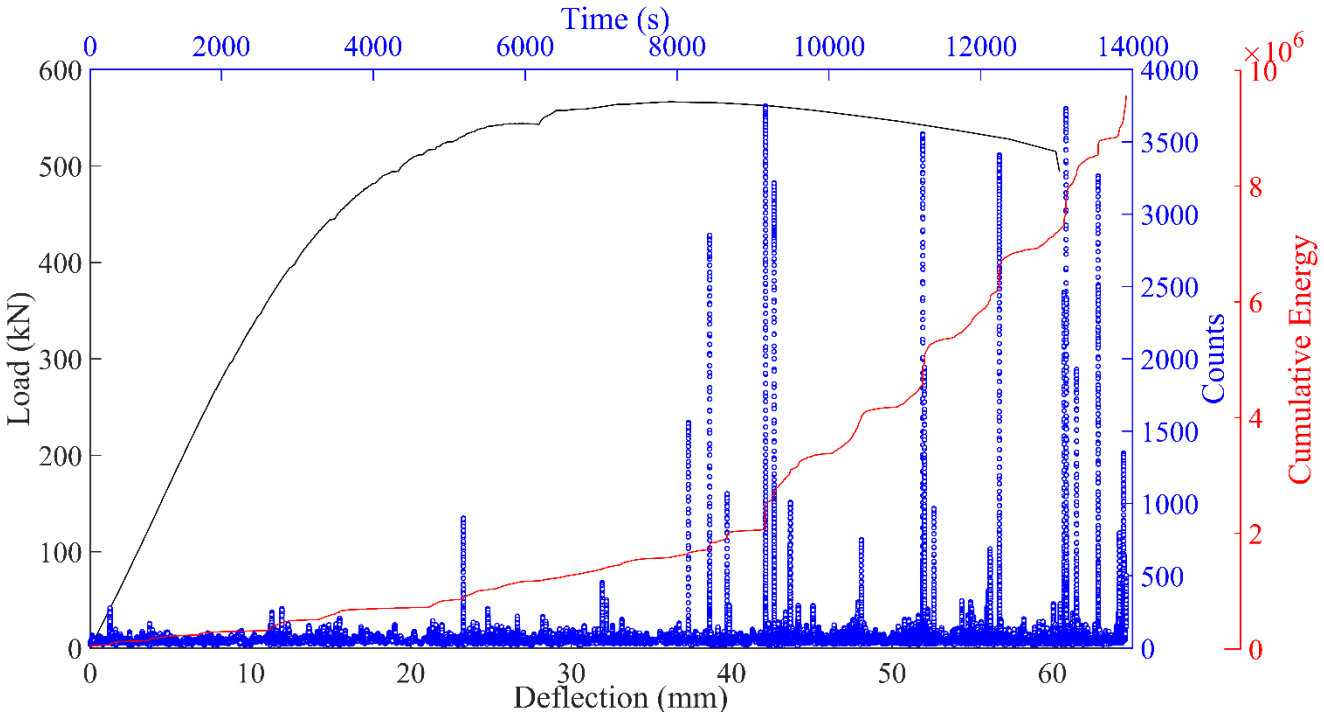

Figure 11: Correlation of load-deflection curve with released AE energy and counts for GC-1

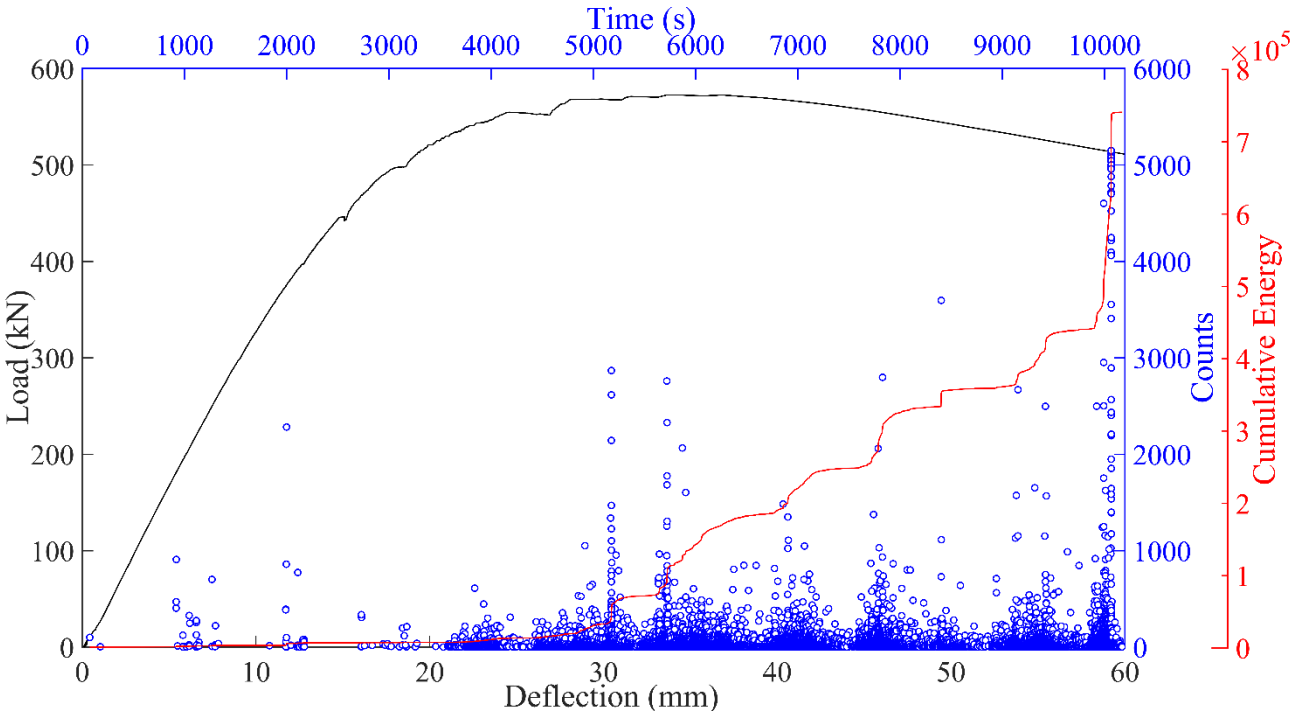

Figure 12: Correlation of load-deflection curve with released AE energy and counts for GC-2

4.2 RMS

Another waveform parameter considered herewith is the RMS. ElBatanouny et al. (2014) highlighted that when failure is imminent, a considerable increase in RMS can be noted. This is due to the fact that RMS is directly related with the signal energy. To demonstrate the correlation of RMS with damage growth within a GC, values corresponding to different stages of the tests are used as shown in Figure 13. The first stages are within the elastic stage; stage 1 corresponds to activity recorded below 100 kN and the second stage contains values recorded at 200-250 kN. In the final stage the AE signals that were recorded after 400 kN are used.

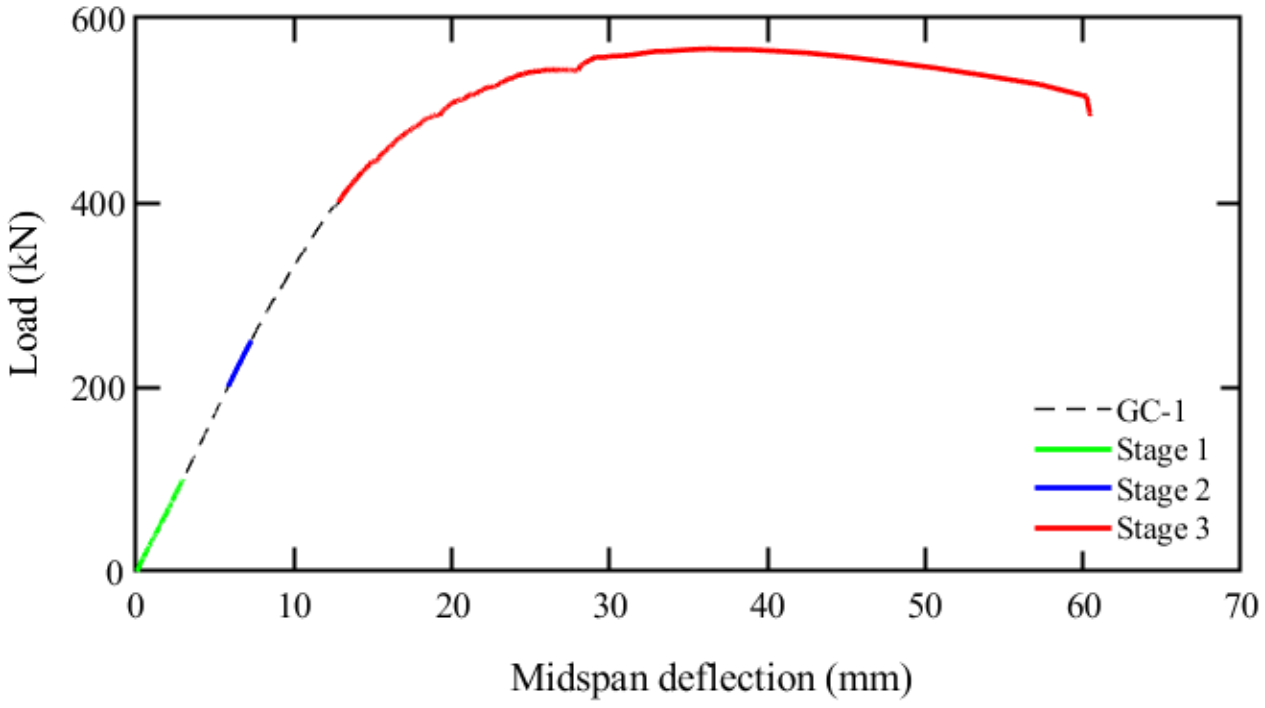

Figure 13: Phases used for RMS analysis

In Figure 14, the RMS is plotted against the peak amplitude for GC-1 (top) and GC-2 (bottom) during three different stages of the flexural test. The three levels were selected considering the findings from the cumulative energy and duration distribution of the events. It is clearly observed that increasing RMS values are recorded once failure becomes imminent. Signal duration and

energy exhibit similar trends with RMS. However, RMS values increased significantly from stages 1 and 2 to the final stage when final failure was imminent. This is due to compressive struts failing progressively after 400 kN for both GCs (Figure 15). This suggests that RMS is an effective KPI for assessing the likelihood of catastrophic failure. The maximum RMS values for both specimens during the three test stages are tabulated in Table 3.

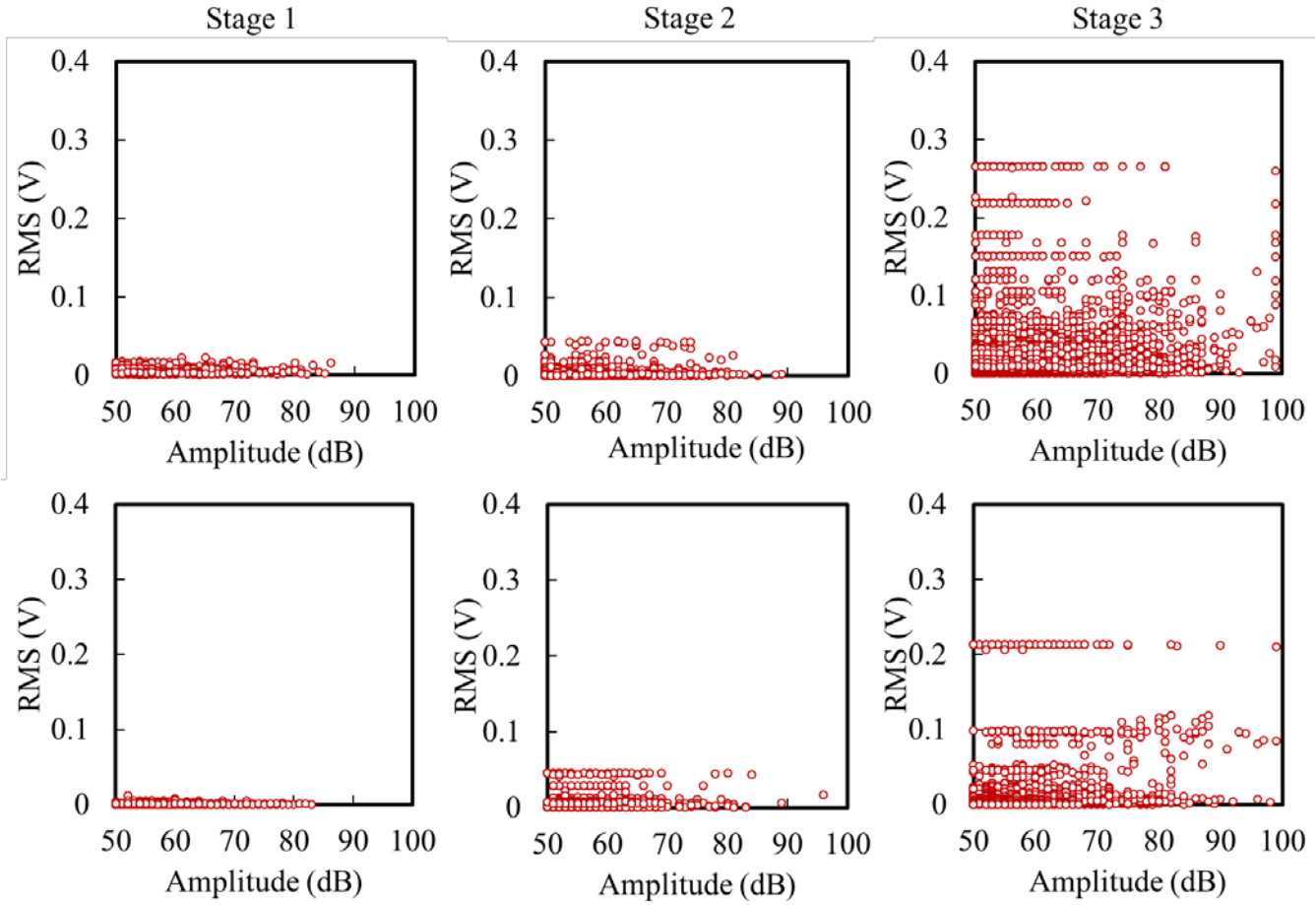

Figure 14: RMS for GC-1 (top) and GC-2 (bottom) at different stages during test

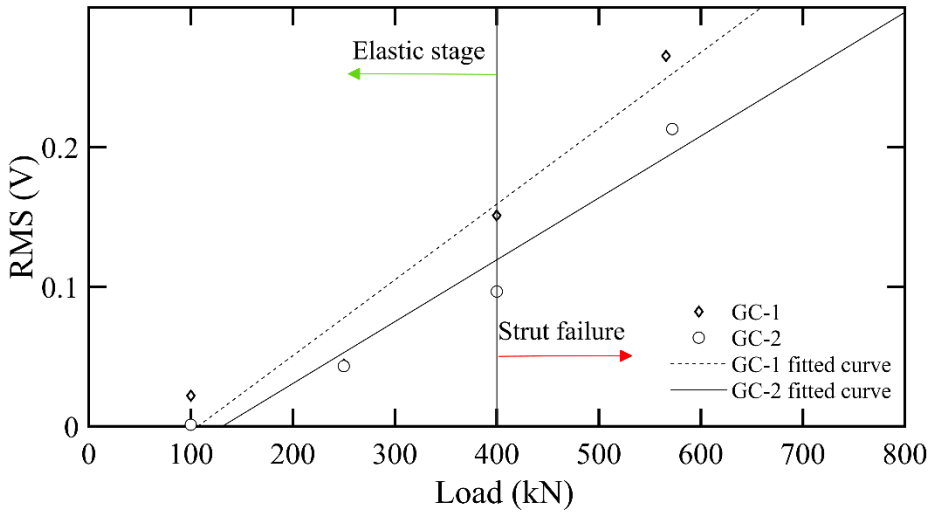

Figure 15: Recorded RMS values during the elastic stage and after strut failure

Table 3: RMS values for GCs during bending tests

Specimen ID	RMS (V)		
	Stage 1	Stage 2	Stage 3
GC-1	0.022	0.0442	0.2654
GC-2	0.0118	0.046	0.2134

5 Crack detection

For GCs with shear keys, cracks are of particular interest as they are associated with strut failure between shear keys. Cracking mainly occurs within the shear key region since those transfer a large proportion of the bending loads. For both specimens it was visually confirmed that cracking of the grout core occurred mainly in the vicinity of the shear keys. The diagonal cracks initiated and propagated between opposing shear keys, to form a cylindrical failure surface. Failure of the diagonal struts occurred progressively at four different load levels (1-4) as shown in Figure 16, during which the interface gap developed until the completion of the test once pile

buckling occurred. Initially, at a load of approximately 396.8 *kN* (12.6 *mm* deflection), followed by level two and three at 442.5 *kN* (15.0 *mm* deflection), 499.7 *kN* (18.6 *mm* deflection) respectively and finally at 543.2 *kN* (28.1 *mm* deflection). This progressive failure sequence of the connections has also been confirmed with finite element investigations (Tziavos et al., 2019). Cracking events are usually associated with high amplitudes, due to the rapid release of energy. Therefore, they are widely used to evaluate the intensity of the emissions and subsequently for damage quantification. The amplitude of each AE signal corresponds to an energy content strongly dependent on the event generating damage, the distance between the event and the sensor as well as the attenuation of the wave (Shiotani et al., 2007). However, previous research by Muralidhara et al. (2010) has highlighted that the magnitude of an elastic wave can vary in energy content. An example is shown in Figure 17, where amplitudes of the same magnitude appear with varying energy. Therefore, isolated peak amplitudes of events must be treated with care as those are not a clear indication of damage.

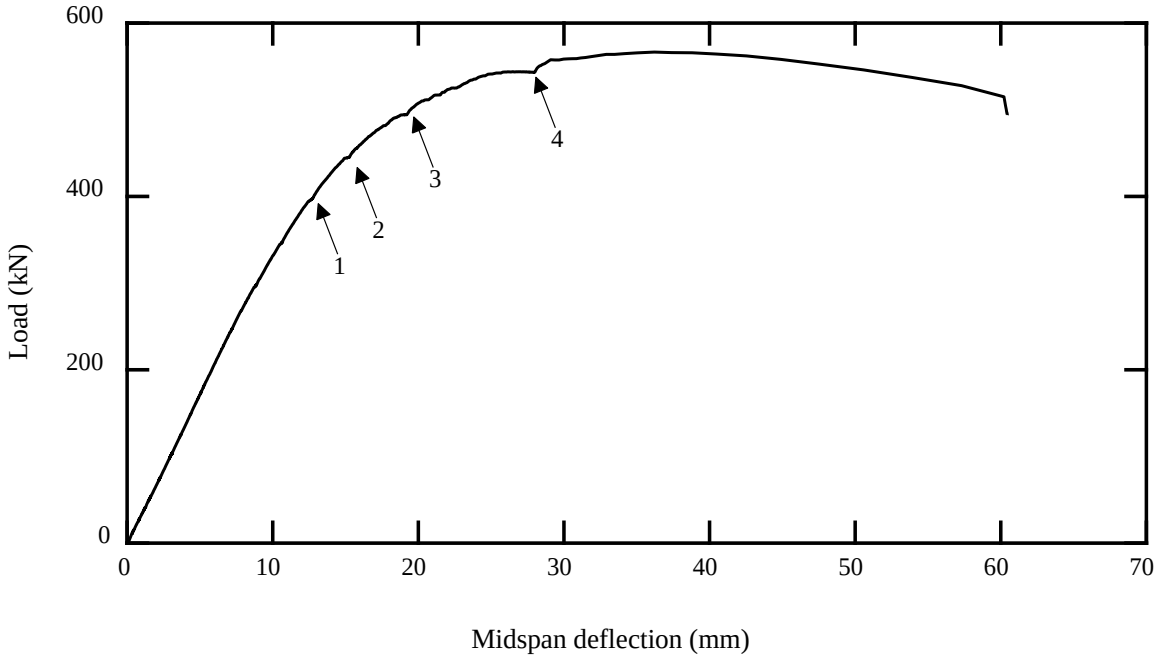

Figure 16: Progressive strut failure on GC-1 specimen

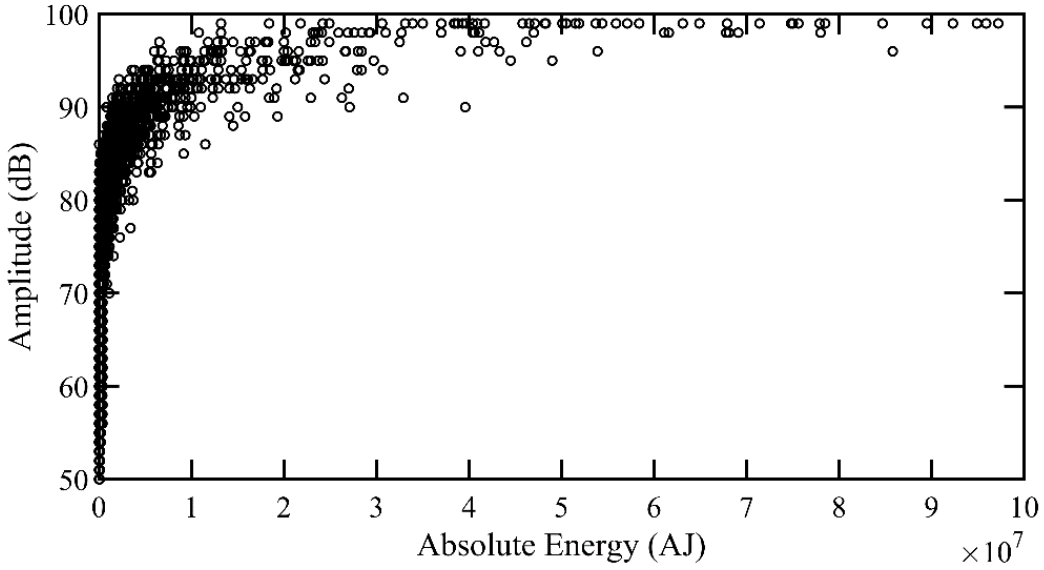

Figure 17: Amplitude against absolute energy (data from AE4 sensor from specimen GC1)

To investigate signal amplitude values, since those contain important information with respect to damage characteristics, alternative statistical approaches can be adopted. A tool which uses the cumulative distribution of the recorded amplitudes is the b-value analysis. The approach has been derived from earth sciences, where it is used to examine seismic events (Gutenberg and Richter, 1956). To do so, the following empirical formula is used:

$$\log_{10}N=a-bM_L \quad (1)$$

where N is the incremental frequency of events within a range of magnitudes, a, b are constants and M_L is the earthquake magnitude.

A feasible application of the seismic b-value has been found to be for the analysis of AE signals. Particularly, when it comes to the fracture of brittle materials such as concrete or rock, promising results have been reported (Sagar and Rao, 2014; Rao and Lakshmi, 2005). For use with AE data sets, equation 1 needs to be modified to include the amplitude in dB divided by a factor (Colombo et al., 2003) so as to allow for comparisons with the seismic b-value as follows:

$$\log_{10}N=a-b\left(\frac{A_{dB}}{20}\right) \quad (2)$$

An interesting characteristic of the calculated *b*-values for brittle materials, especially when failure is approaching is that significantly lower values occur, indicating macrocrack formation. This has been extensively reported in the relevant literature (e.g., Farhidzadeh et al., 2013; Sagar and Rao, 2014; Frohlich and Davis, 1993; Kurz et al., 2006). The relationship between increasing stresses and *b*-values appears to be inversely proportional (Rao and Lakshmi, 2005). Typical *b*-values range from 2.5 in early stages, to values below 1 closer to failure (Colombo et al., 2003).

The study of the slope of the linear fit of the cumulative frequency distribution of signal amplitude with respect to magnitude, provides a good indication of imminent fracture. However, the relationship is not always linear. For this reason, Shiotani et al. (1994) suggested an improved b-value which involves statistical measures of the data set, namely the mean amplitude and standard deviation of the distribution. For the computation of the improved b-value equation 3 is used:

$$Ib=\left(\frac{\log N(\mu-\alpha_1\sigma)-\log N(\mu-\alpha_2\sigma)}{(\alpha_1+\alpha_2)\sigma}\right) \quad (3)$$

where μ is the mean amplitude value, σ the standard deviation and α_1, α_2 are user-defined constants. Following this, PAC also developed a dedicated software for *Ib*-value calculation which allows the use of the peak amplitude or the energy as input:

$$Ib=\left(\frac{\log N_1-\log N_2}{a_1-a_2}\right) \quad (4)$$

where $a_1 = \mu - \alpha_1\sigma$, $a_2 = \mu + \alpha_2\sigma$ while $\alpha_1$and α_2 ranges from 0.5 to 5.

5.1 b and Ib-value analysis

To detect cracking events during the bending tests, the *b* and *Ib*-value analysis were performed as described in the previous section. The computations were performed using complete time series unless stated otherwise. The peak amplitudes were divided in small-ranged bins from the set-threshold to 100 dB with a magnitude of 5dB forming group of events. A sliding function of 50 events was used in order to trace all important events. In order to calibrate the optimum number of events within each group several trials were performed to ensure results are independent of selected group size. This was initially noted by Colombo et al. (2003). A comparison for both approaches using a varying event number is presented in Figure 18, where 500 seconds of the GC-1 test are used for demonstration purposes. As the sliding function and number of events of each group were found not to affect the results, groups formed by 150 events were chosen for the following analysis.

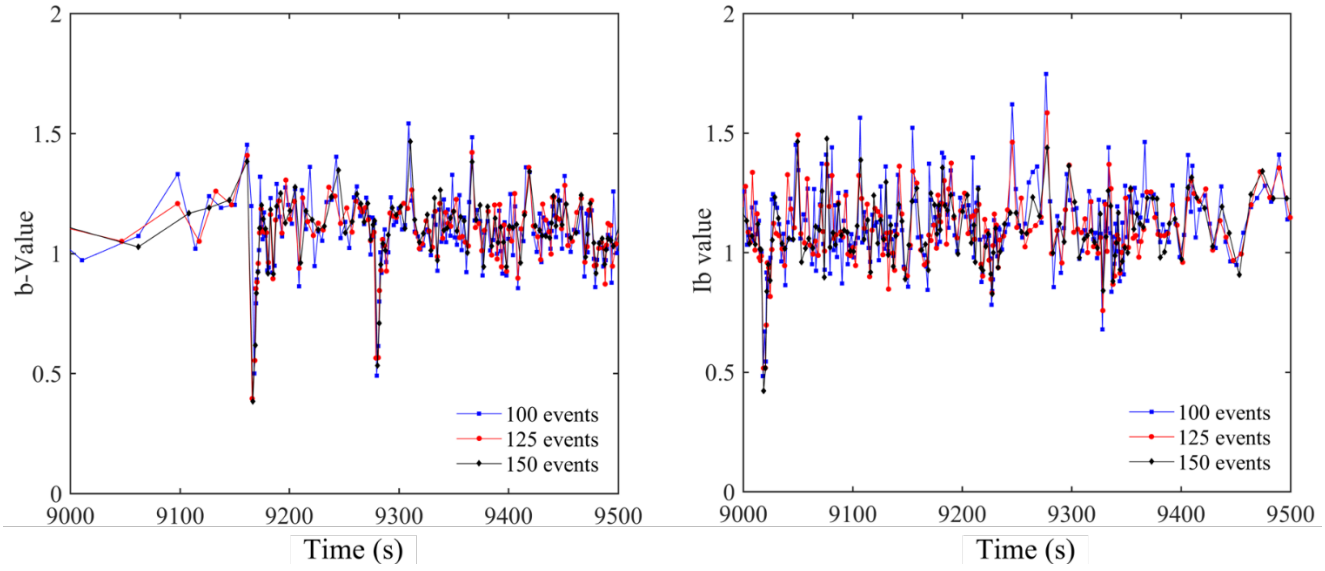

Figure 18: Effect of event number on *b* (left) and *Ib*-value (right)

Both methods are shown in Figure 19 for GC-1. It is evident that similar trends are observed for both approaches. The resulting time series of the two computations contain a large

number of data points as the only filtering that was performed was the removal of AE signals with zero PAC energy values. The average *b* value is close to 1 as expected. However, when such analysis is performed the main areas of interest are those where peaks or drops of the gradient occur. These can be associated with damage events of high importance, such as cracking in the present case. Peaks are commonly associated with microcrack formation and drops with the transition to macrocrack growth and crushing of cementitious material.

After the first 4000 s, some peaks and drops are emerging. The *Ib*-value extremes are slightly more pronounced for the whole time series. Also, the notion that the gradient of the slope reduces dramatically once failure is upcoming can be confirmed considering the patterns after 8000 *s*. The density of events increased significantly while distinct drops well below the average value of 1 are observed in both methods. As the trends of the two methods appeared to produce similar results for the remaining sections only *Ib*-value will be considered.

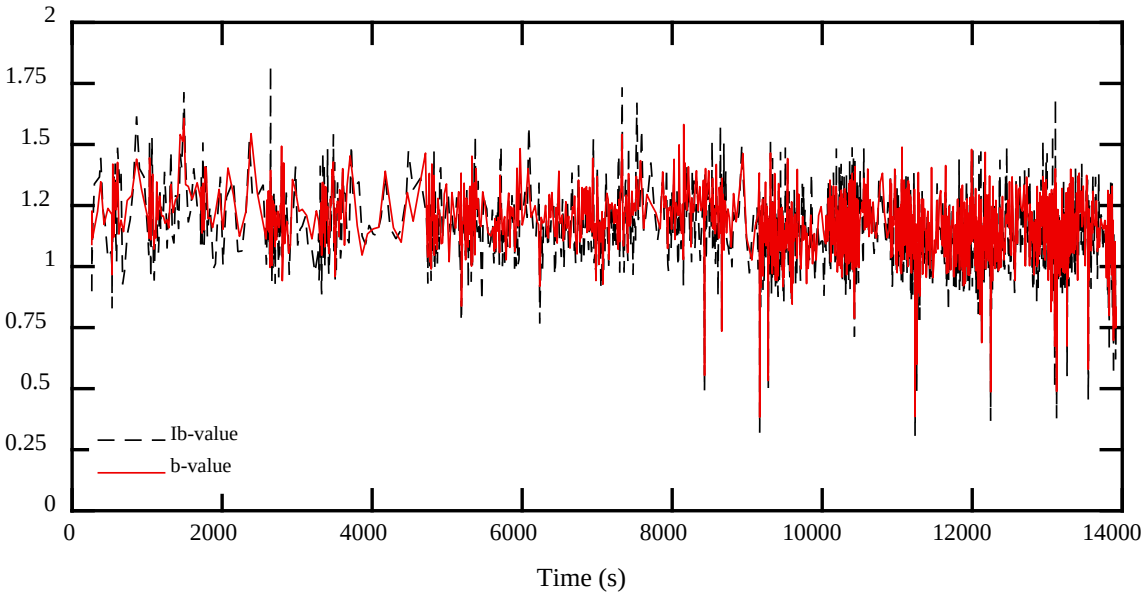

Figure 19: Comparison between *b* and *Ib*-value for GC-1

To highlight major peak and drops, an envelope of the local maximum and minimum *Ib*-values is plotted against the load level (Figure 20). The load level corresponds to the load at the time of interest normalised against the ultimate load sustained by the GC. The extreme values of *Ib* enable the identification of different damage states within the connection in a quantitative way. During phase I, values up to 1.824 were found, while in phase II the *Ib*-value dropped from 1.671 to 0.306 and a number of drops are captured. During the last phase (III) of the test, distinct drops resulting in low values were also recorded until final failure of the specimen. In Colombo et al. (2003) similar trends and magnitudes were reported. It is suggested that high values are related with microcracking and due to the load-transfer mechanism within the shear key region, whereas after the elastic stage the formation of failure surfaces between opposing shear keys leads to drops in *Ib* values. It is worth noting that the drops associated with cracks are dependent on the selected specimen geometry and the progressive failure sequence that was observed during the tests.

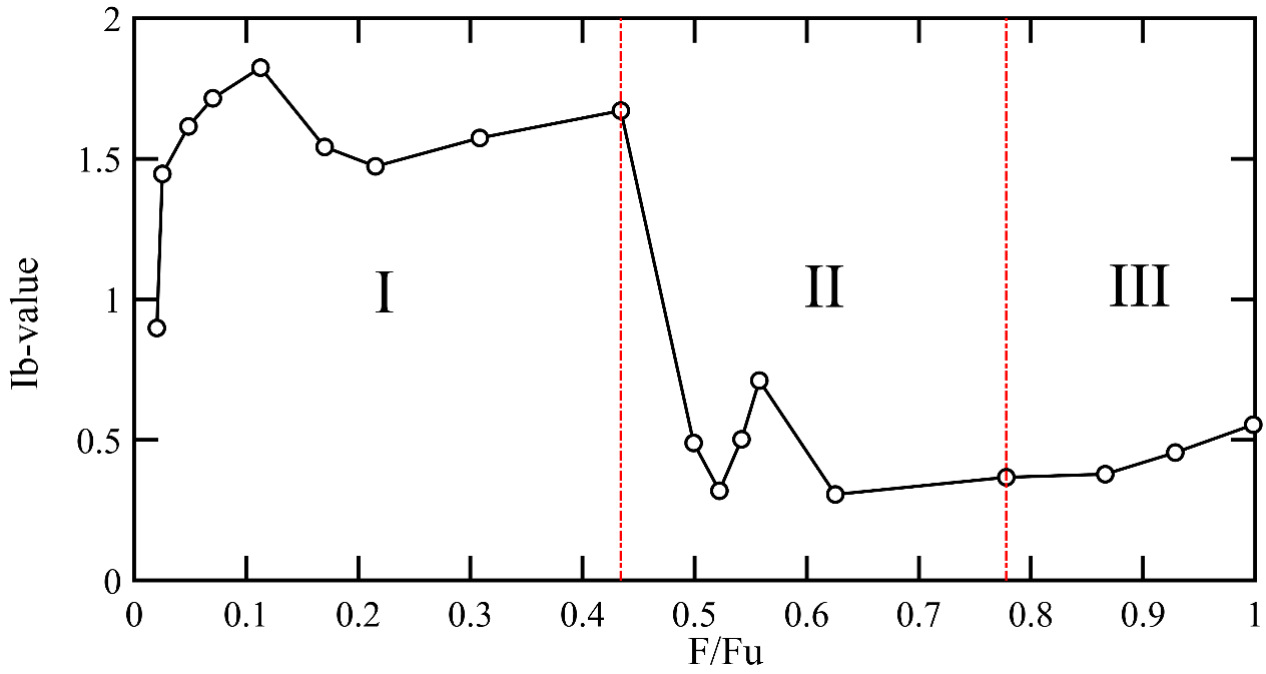

Figure 20: Peaks and drops of *Ib*-value for GC-1

In order to verify that the sudden drops in *Ib*-value are associated with events of high energy release, the findings from *Ib*-value analysis are compared with the rate of CSS. CSS is interconnected with energy and exhibited a similar exponential trend with the increasing load on the GC (Figure 21).

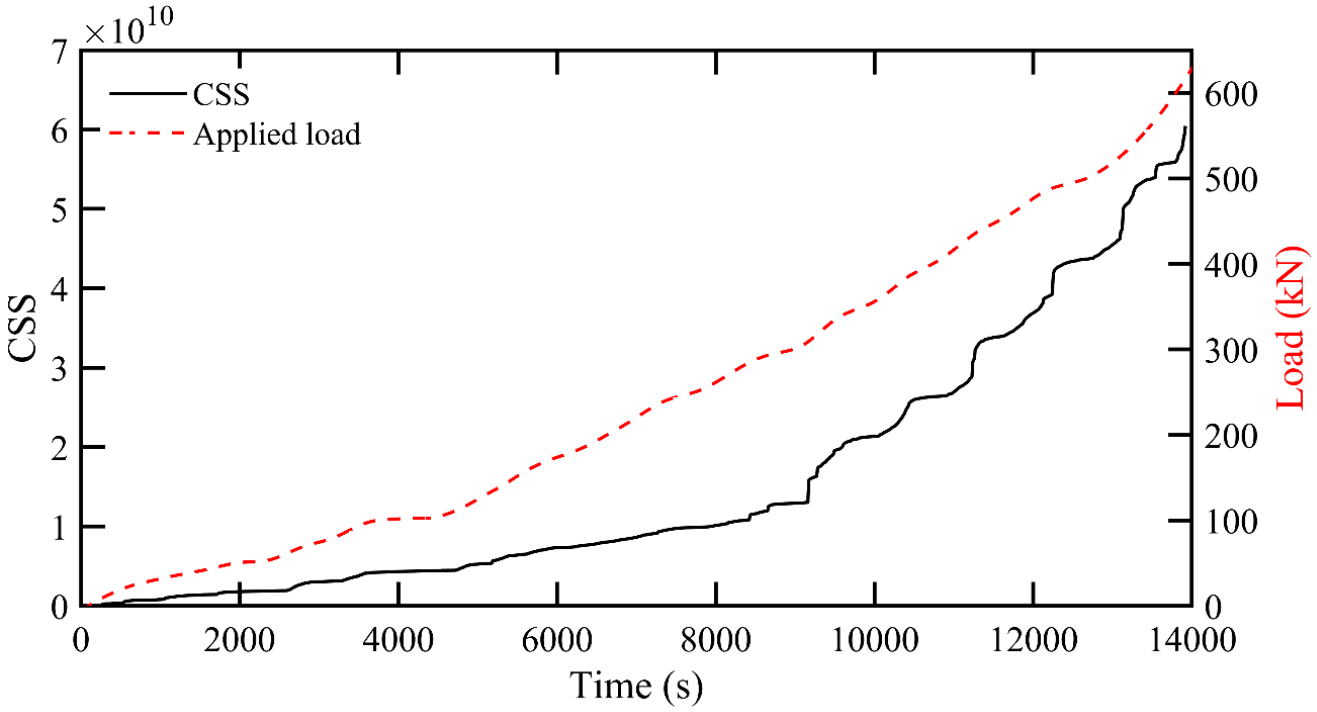

Figure 21: Cumulative signal strength against applied load

A comparison of the CSS growth rate and *Ib* values during the final stages of the test were the majority of damage occurred are shown in Figure 22. The results depict an excellent agreement between the two parameters suggesting that events of high-energy release such as cracking are accurately capture with the Ib-value analysis. The trends of *Ib*-value have been also compared with the rise-time-amplitude (RA) ratio values. RA is often employed to investigate the type of fracture of brittle materials and more often in concrete. It is computed as follows:

$$RA = \left(\frac{\text{Rise time}}{\text{Amplitude}}\right) \quad (5)$$

As depicted in Figure 23 the macrocrack formation which is suggested from the *Ib*-value drops well below unity, coincides with the peaks in RA values. To summarise the above, it is suggested that RA ratio, CSS, RMS are important KPIs along with the statistical analysis of the amplitude distribution.

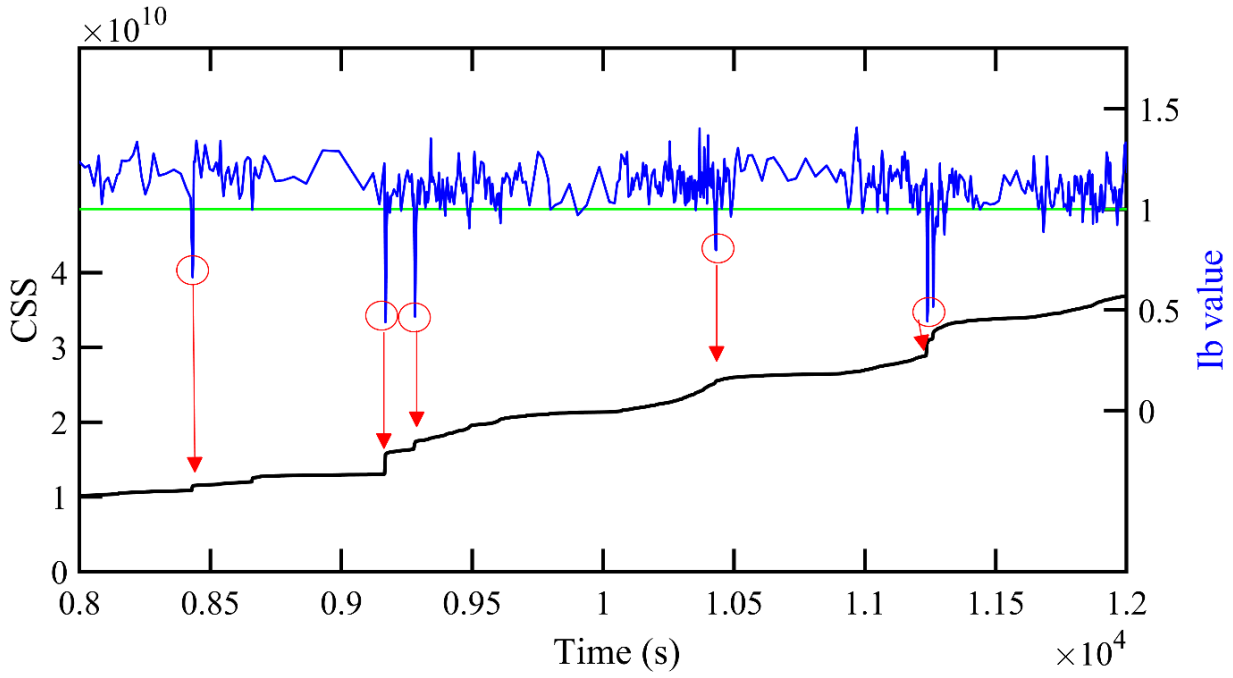

Figure 22: CSS and *Ib*-value correlation

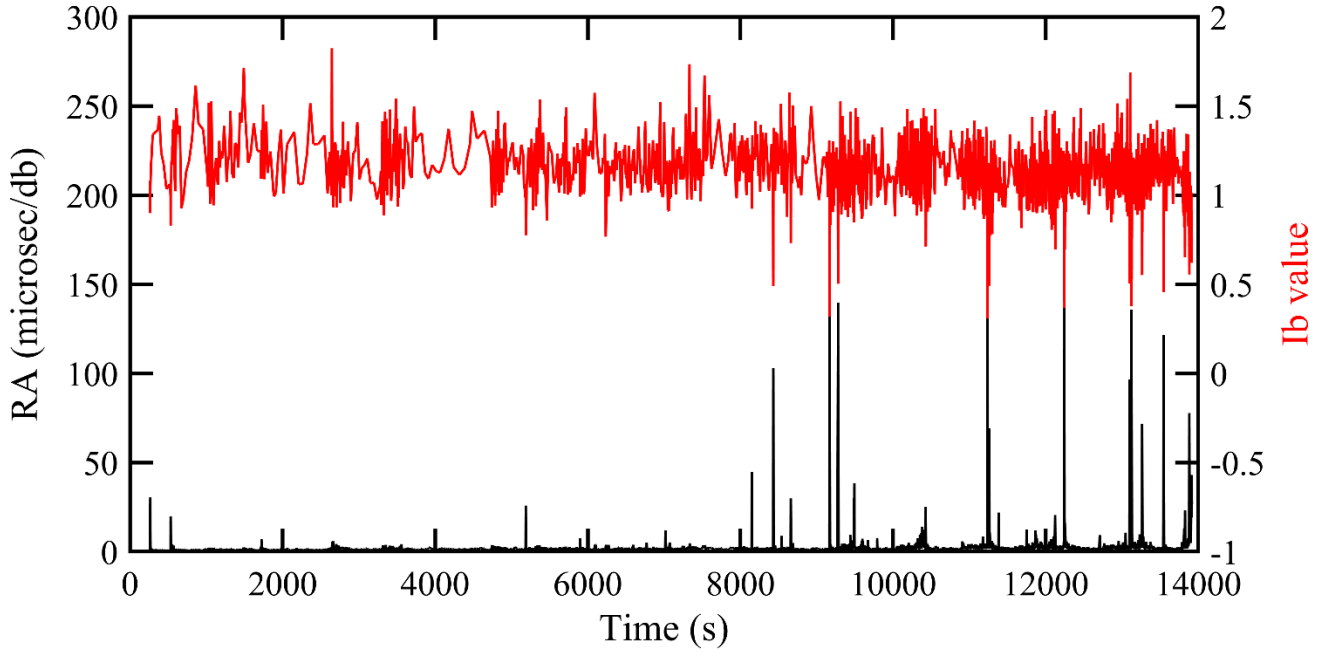

420

421 Figure 23: Correlation of *Ib*-value and RA

422

6 Summary and Conclusions

This paper presented the results of an experimental study on the application of AE on GCs under bending loads. An investigation on several AE parameters has been carried out in order to single out those that are more sensitive to failure and could be used as KPI for damage assessment. Finally, the use of *b* and *Ib*-value was also examined as a tool for crack detection. The following conclusions have been drawn from the presented experimental work:

- The applicability of AE for monitoring OWTs substructures was confirmed in laboratory-scaled GCs. It was shown that the number of events and the duration of the AE signals are potential KPIs for damage growth.
- RMS is one of the KPIs that can be implemented in monitoring tools to act as a prognosis for hindering failures mainly associated with the integrity of the grout. RMS values revealed stable magnitude levels while the GC remained in the elastic stage. Pronounced increases occurred for both specimens once 50% of the capacity was reached. RMS cross plots revealed similar trends for both specimens.
- RA ratios along with CSS rates can be effectively used to isolate cracking events within a GC and are also classified as KPIs.
- Cracking events with high energy release were satisfactorily captured and associated with drops in both *b* and *Ib*-value. Correlation of steep drops with failure modes of the specimen was possible when compared with CSS, RA and visual inspections. Hence, it was shown that for both *b* and *Ib*-value steep drops occur closer to events of significance and the approach can be used for crack detection.
- One of the challenges of the presented approach was the optimum setting of the acquisition parameters employed. This is due to the size of the specimens and test supports which could potentially lead to increased scattering of AE waves. It is also

suggested that the presence of micro-voids and aggregates of varying diameters within the material leads to a large number of AE signals.

Further tests are needed employing materials of different strengths and at varying ambient conditions, to enhance the reliability of the obtained results for quantifying damage in OWT substructures accurately.

Acknowledgments

The authors would like to acknowledge Densit® for providing the grout material used in this study. In addition, the support of the European Commission's Framework Program "Horizon 2020" through the Marie Skłodowska-Curie Innovative Training Networks (ITN) "AEOLUS4FUTURE - Efficient harvesting of the wind energy" (H2020-MSCA-ITN-2014: Grant agreement no. 643167) and the COST Action TU1804 WINERCOST – "Wind Energy to enhance the concept of Smart cities" is gratefully acknowledged. The first author acknowledges the funding provided by the School of Engineering at the University of Birmingham, UK

References

Aggelis, D. G. (2011). Classification of cracking mode in concrete by acoustic emission parameters. Mechanics Research Communications, 38(3), pp. 153-157. https://doi.org/10.1016/j.mechrescom.2011.03.007

Artigao, E., Martin-Martinez, S., Honrubia-Escribano, A., Gomez-Lazaro, E. (2018). Wind turbine reliability: A comprehensive review towards effective condition monitoring. Applied Energy, 228, pp. 1569-1583. https://doi.org/10.1016/j.apenergy.2018.07.037

Behnia, A., Chai, H.K. & Shiotani T. (2014). Advanced structural health monitoring of concrete structures with the aid of acoustic emission. Construction and Building Materials, 65, pp. 282-302. https://doi.org/10.1016/j.conbuildmat.2014.04.103

Brett, C. R., Gunn, D. A., Dashwoo, B. A. J., Holyoake, S.J. and Wilkinson, P. B. (2018). Development of a technique for inspecting the foundations of offshore wind turbines. Insight - Non-Destructive Testing and Condition Monitoring, 60(9), pp. 19-27. https://doi.org/10.1784/insi.2018.60.1.19

BSI, (2009). BS EN 12390-3:2009: Testing hardened concrete. Compressive strength of test specimens.

Chen, T., Li, Z., Wang, X., Yuan, G. and Liu, J. (2018). Experimental study on ultimate bending performance of grouted connections in offshore wind turbine support structures. Thin-Walled Structures, (132), pp. 522-536. https://doi.org/10.1016/j.tws.2018.09.025

Colombo, I. S., Main, I. G. and Forde, M. C. (2003). Assessing damage of reinforced concrete beam using "b-value" analysis of acoustic emission signals. Journal of materials in civil engineering, 15(3), pp. 280-286. https://doi.org/10.1061/(ASCE)0899-1561(2003)15:3(280)

Dallyn, P., El-Hamalawi, A., Palmer, A. and Knight, R. (2016). Experimental teting of grouted connections for offshore substructures: A critical review. Structures, 3, pp. 90-108. https://doi.org/10.1016/j.istruc.2015.03.005

Densit (2018). Technical data sheet -Ducorit©. Ultra-High Performance Grout. Aalborg, Denmark. Available at: http://densit.com/media/27259/pro-ducorit-uk.pdf [Accessed at: 05/07/2018].

Duthie, D. B. and Gabriels, F. (2014). Remote Monitoring of Offshore Structures using Acoustic Emission. *In*: European Conference on Non-Destructive Testing (ECNDT), Prague, Czech Republic.

ElBatanouny, M. K., Larosche, A., Mazzoleni, P., Ziehl, P. H., Matta, F. and Zappa, E. (2014). Identification of Cracking Mechanisms in Scaled FRP Reinforced Concrete Beams using Acoustic Emission. Experimental Mechanics, 54, pp. 69-82. https://doi.org/10.1007/s11340-012-9692-3

Farhidzadeh, A., Dehghan-Niri, E., Salamone, S., Luna, B. and Whittaker, A. (2013). Monitoring crack propagation in reinforced concrete shear walls by acoustic emission. Journal of Structural Engineering, 139(12), pp. 04013010. https://doi.org/10.1061/(ASCE)ST.1943-541X.0000781

Frohlich, C. and Davis, S. D. (1993). Teleseismic b values; or much ado about 1.0. Journal of Geophysical Research: Solid Earth, 98(B1), pp. 631-644.

Grosse, C. U. and Ohtsu, M. (2008). *Acoustic Emission Testing*. Springer Science & Business Media. https://doi.org/10.1007/978-3-540-69972-9

Gutenberg, B. and Richter, C. F. (1956). Earthquake magnitude, intensity,, energy, and acceleration (second paper). Bulletin of the seismological society of America, 46(2), pp. 105-145.

Häckell, M., Friedmann, H. and Feulner, M. (2017). Detecting damage in grouted-joints of wind turbine support structures – application to a large-scale experiment. In: 11th I*nternational*

505 *workshop on structural health monitoring*, Stanford, USA, 2017, pp.2467–2474. DEStech
506 Publications, Inc.

507 Iliopoulos, A. N., Van Helerijck, D., Vlassenbroeck, J. and Aggelis, D. G. (2016). Assesment of
508 grouted samples from monopile wind turbine foundations using combined non-destructive
509 techniques. Construction and Building Materials, 122, pp. 855-862.
510 https://doi.org/10.1016/j.conbuildmat.2015.11.047

511 Jungert, A. (2008). Damage Detection in wind turbine blades using two different acoustic
512 techniques. The NDT Database & Journal *(NDT)*.

513 Kurz, J. H., Finck, F., Grosse, C. U. and Reinhardt, H. W. (2006). Stress drop and stress
514 redistribution in concrete quantified over time by the b-value analysis. Structural health
515 monitoring, 5(1), pp. 69-81. https://doi.org/10.1177/1475921706057983

516 Li, D., Du, F. and Ou, J. (2017). Damage evaluation of fiber reinforced plastic-confined circular
517 concrete-filled steel tubular columns under cyclic loading using the acoustic emission technique.
518 Smart Materials and Structures, 26, pp. 1-13. https://doi:10.1088/1361-665X/aa57c9

519 Lotsberg, I. (2013). Structural mechanics for design of grouted connections in monopile wind
520 turbine structures. Marine Structures, 32, pp. 113-135.
521 https://doi.org/10.1016/j.marstruc.2013.03.001

522 Marion, S., Johansen, A., Solland, G. and Nybø, T. (2018). Testing of jacket pile sleeve grouted
523 connections exposed to shear forces and bending moments. Marine Structures, 59, pp. 401-422.
524 https://doi.org/10.1016/j.marstruc.2018.02.008

Márquez, F. P. G., Perez, J. M. P., Marugan, A. P. and Papaelias, M. (2016). Identification of critical components of wind turbines using FTA over the time. Renewable Energy, 87, pp. 869-883. https://doi.org/10.1016/j.renene.2015.09.038

Márquez, F. P. G., Tobias, A. M., Perez, J. M. P. and Papaelias, M. (2012). Condition monitoring of wind turbines: Techniques and methods. Renewable Energy, 46, pp. 169-178. https://doi.org/10.1016/j.renene.2012.03.003

Martinez-Luengo, M., Kolios, A. and Wang, L. (2016). Structural Health Monitoring of offshore wind turbines: A review through the Statistical Pattern Recognition Paradigm. Renewable and Sustainable Energy Reviews, 64, pp. 91-105. https://doi.org/10.1016/j.rser.2016.05.085

Marugán, P. A., Márquez, F. P. G. and Pérez, J. P. (2016). Optimal maintenance management of offshore wind farms. Energies, 9(1), pp.46. https://doi.org/10.3390/en9010046

Moll, J. (2018). Damage detection in grouted connections using electromechanical impedance spectroscopy. Proceedings of the Institution of Mechanical Engineers – Part C: Journal of Mechanical Engineering Science. https://doi.org/10.1177/0954406218764226

Muralidhara, S., Prashad, R. B. E. H. and Karihaloo, B. L. (2010). Fracture process zone size and true fracture energy of concrete using acoustic emission. Construction and Building Materials, Volume 24, pp. 479-486. https://doi.org/10.1016/j.conbuildmat.2009.10.014

Rao, M. V. M. S. and Lakshmi, K. J. P. (2005). Analysis of b-value and improved b-value of acoustic emissions accompanying rock fracture. Current Science, 89(9), pp. 1577-1582.

Rolfes, R., Tsiapoki, S. and Häckell, M. W. (2014). Sensing solutions for assessing and monitoring wind turbines. Sensor technologies for civil infrastructures: Applications in Structural Health

546 Monitoring. Woodhead Publishing Series in Electronic and Optical Materials, pp. 565-604.
547 https://doi.org/10.1533/9781782422433.2.565

548 Sagar, R. V. and Rao, M. V. M. S. (2014). An experimental study on loading rate effect on acoustic
549 emission based b-values related to reinfroced concrete fracture. Construction and Building
550 Materials, Volume 70, pp. 460-472. https://doi.org/10.1016/j.conbuildmat.2014.07.076

551 Shafiee, M. and Sorensen, J. D. (2017). Maintenance optimization and inspection planning of wind
552 energy assets: Models, methods and strategies. Reliability Engineering and System Safety, pp. 1-
553 19. https://doi.org/10.1016/j.ress.2017.10.025

554 Shafiee, M., Brennan, F. and Espinosa, I. A. (2016). A parametric whole life cost model for offshore
555 wind farms. International journal Life Cycle Assessment, 21(7), pp. 961-975.
556 https://doi.org/10.1007/s11367-016-1075-z

557 Shi, S., Han, Z., Liu, Z., Vallely, P., Soua, S., Kaewunruen, S. and Papaelias, M., (2018).
558 Quantitative monitoring of brittle fatigue crack growth in railway steel using acoustic emission.
559 Proceedings of the Institution of Mechanical Engineers, Part F: Journal of Rail and Rapid Transit,
560 232(4), pp.1211-1224. https://doi.org/10.1177/0954409717711292

561 Shiotani, T. (1994). Evaluation of progressive failure using AE sources and improved b-value on
562 slope model tests. Progress in Acoustic Emission *VII*, 7, pp.529-534.

563 Shiotani, T., Aggelis, D. G. and Makishima, O. (2007). Global monitoring of concrete bridge using
564 acoustic emission. Journal of acoustic emission, 25, pp. 308-315.

565 Tziavos, N. I. (2019). Experimental and numerical investigations on grouted connections for
566 monopile offshore wind turbines. Doctoral dissertation, Department of Civil Engineering,
567 University of Birmingham, UK.

568 Tziavos, N. I., Hemida, H., Metje, N. and Baniotopoulos, C. (2016). Grouted connections on offshore
569 wind turbines: a review. Proceedings of the Institution of Civil Engineers - Engineering and
570 Computational Mechanics, 169(4), pp. 183-195. https://doi.org/10.1680/jencm.16.00004

571 Tziavos, N.I., Hemida, H., Metje N. and Baniotopoulos, C. (2019). Non-linear finite element
572 analysis of grouted connections on monopile wind turbines. Ocean Engineering, 171, pp. 633-645.
573 https://doi.org/10.1016/j.oceaneng.2018.11.005

574 Wilke, F. (2013). Load Bearing Behaviour of Grouted Joints Subjected to Predominant Bending.
575 Doctoral Dissertation, Institute for Steel Construction, Leibniz Universität Hannover, Hannover,
576 Germany.

577 Yang, W., Court, R., Jiang, J. (2013). Wind turbine condition monitoring by the approach of
578 SCADA data analysis. Renewable Energy, 53, pp. 365-376.
579 https://doi.org/10.1016/j.renene.2012.11.030